

# Pixel-Level Feature Extraction Model for Breast Cancer Detection

Nishant Behar\* and Manish Shrivastava

Guru Ghasidas Vishwavidyalaya, Bilaspur, 45009, India

\*Corresponding Author: Nishant Behar. Email: nishant.itggv@gmail.com

Received: 01 May 2022; Accepted: 27 June 2022

**Abstract:** Breast cancer is the most prevalent cancer among women, and diagnosing it early is vital for successful treatment. The examination of images captured during biopsies plays an important role in determining whether a patient has cancer or not. However, the stochastic patterns, varying intensities of colors, and the large sizes of these images make it challenging to identify and mark malignant regions in them. Against this backdrop, this study proposes an approach to the pixel categorization based on the genetic algorithm (GA) and principal component analysis (PCA). The spatial features of the images were extracted using various filters, and the most prevalent ones are selected using the GA and fed into the classifiers for pixel-level categorization. Three classifiers—random forest (RF), decision tree (DT), and extra tree (ET)—were used in the proposed model. The parameters of all models were separately tuned, and their performance was tested. The results show that the features extracted by using the GA+PCA in the proposed model are influential and reliable for pixel-level classification in service of the image annotation and tumor identification. Further, an image from benign, malignant, and normal classes was randomly selected and used to test the proposed model. The proposed model GA-PCA-DT has delivered accuracies between 0.99 to 1.0 on a reduced feature set. The predicted pixel sets were also compared with their respective ground-truth values to assess the overall performance of the method on two metrics—the universal image quality index (UIQI) and the structural similarity index (SSI). Both quality measures delivered excellent results.

**Keywords:** Breast cancer; machine learning; classification; feature extraction; feature selection

## 1 Introduction

Cancer is caused by cell abnormalities and is a leading cause of death worldwide. The American Cancer Society (ACS) has estimated that 1.9 million new cancer cases were identified and 608,570 people died of the disease in 2021 in the United States alone (1670 deaths/day) [1]. Breast cancer is the most frequently diagnosed form of cancer [2]. Breast cancer detection is an important but difficult task because symptoms of the disease are not prominent in the early stages. A commonly used technique for detecting cancer is the fine-needle aspiration (FNA) procedure, in which tissues are collected from



This work is licensed under a Creative Commons Attribution 4.0 International License, which permits unrestricted use, distribution, and reproduction in any medium, provided the original work is properly cited.

areas of the body that are likely to be afflicted. FNA is an invasive and painful process but provides accurate results. The extracted tissues are fixed into slides, and the cytoplasm and nuclei are highlighted in different colors through hematoxylin and eosin (H&E) staining. These slides are manually analyzed under a microscope to look for abnormalities that are indicative of cancer. Large digitalized images of these slides are usually obtained at a high resolution, and contain colors of different intensities in different parts. Analyzing the entire image of a slide is time-consuming and, labeling each malignant area is challenging and tedious. Multiple specialists analyze the same images in complex cases and discuss their opinions to reach a consensus. These experts may have different opinions on artifacts present in the same image. Their final diagnoses can differ, and depend on their level of expertise. Computer-aided diagnostics (CAD) systems can be used to analyze digital images by using computer vision and image processing methods. This study proposes an automatic machine learning (ML) based model for the pixel categorization and labeling of images for the diagnosis of breast cancer.

The remainder of this paper is organized into the following sections: Section 2 describes past work in the area of image segmentation, feature extraction, and machine learning. Section 3 details the proposed method, which includes the random forest (RF), decision tree (DT) and extra tree (ET) algorithms as well as feature extraction, genetic algorithm (GA)-based feature selection, and performance-related parameters. Section 4 describes the experimental setup used to test the proposed method, the results, and an assessment of its performance. Section 5 summarizes the conclusions of this study and highlights directions for future work in the area.

## 2 Literature Review

Researchers have explored solutions for a better, faster, and more accurate understanding of medical images by using computer-based methods. Medical images contain complex patterns that make image processing tasks challenging. In the last decade, many attempts have been made to detect objects in images. Object-oriented algorithms, firefly models, and hybrid models have been developed for the segmentation and classification of nuclei. A recent study [3] extracted the color histogram as well as features of texture and the frequency domain from RGB images to identify periocular cancer. Another study [4] used four hybrid algorithms for segmentation: K-means, fuzzy C-means, the comparative learning-based neural network, and Gaussian mixture. The competitive learning method attained the highest accuracy (96%) among them. The authors applied the Inception v3 model for feature extraction in a study on the segmentation of lesions [5], extracted gradient-based features from dermoscopic images, and used them for classification with an accuracy of 99.2%. Yet another study [6] used CAD for the detection of skin cancer and extracted unique features from the segmented images of lesions. Lesions in the case of melanoma exhibit variations in color while benign skin has a uniform color. Therefore, color-, shape-, and texture-based features are commonly extracted from images of the skin for diagnosis. The extracted features are then processed to reduce noise in them as well as their dimensionality. A popular method for region segmentation involves identifying pixels with similar values. Researchers [7] have proposed an object-oriented method for measuring the homogeneity of images obtained during the biopsy of the colon by using the distributions of objects in the images. The texture is a fundamental and low-level characteristic that is used to discern the contents and patterns in an image. These characteristics are beneficial for partitioning distinct regions that have the same color. Textural characteristics in ultrasound images are used to diagnose prostate cancer [8–10]. The textural analysis of PET images has also been explored [11], and the authors concluded that textural characteristics are beneficial for tumor detection. Geometric characteristics have been used to locate the internal cervical OS [12]. A study [13] used high-order spectra (HOS) and the local binary pattern (LBP) to identify cases of oral cancer. The authors [14] have utilized an ultrasound scanner to

analyze the textural properties of images to identify cysts. They found that the co-occurrence matrix was suitable for this task. moreover a study [15] retrieved color-and texture-based characteristics from images of patients with meningioma. A study on segmentation [16] focused on detecting breast cancer lesions using texture descriptors. Another studies [17,18] exhibited textural characteristics collected from sub-images to classify breast cancer as benign or malignant. These textural elements were used to obtain average values of images with the same distances between pixels in four distinct orientations. In the reference [19], textural characteristics have been extracted using different filters, the gray-level co-occurrence matrix, and the local properties of images. The feature set thus obtained was used for computer-based breast cancer screening. Traditional techniques of classification include statistical analysis, support vector machine (SVM), artificial neural network (ANN), decision tree (DT), random forest (RF), and K-nearest neighbor (KNN). In a primary study [20], the authors applied four classifiers—one-nearest neighbor (1NN), quadratic linear analysis (QDA), SVM, and RF—to classify histological images of tumors in the breast ether as benign or malignant. Another study [21] assessed the performance of the KNN and ANN classifiers, where the latter outperformed the former. A research paper [22] experimented with a KNN classifier to extract shape-and co-occurrence-based features from a mammography dataset for classification. This method attained an accuracy of 82% under the ROC curve, which is unsatisfactory. Researchers [23] have also developed an automated system for cancer diagnosis and classification by using images obtained during biopsies. It covers a range of necessary tasks from pre-processing to classification, where adaptive histogram equalization was used in the pre-processing, K-means clustering was used for segmentation, and the fuzzy KNN, SVM, and RF algorithms were used for classification. The results of their experiments showed that the KNN is the most accurate model. In recent work, the authors segmented images of the lung and identified the airway in it by using morphological operations. They reduced error by using optimal thresholding on grayscale images [24].

Although the above results are promising there is still room for improvement in feature extraction and reduction in the relevant methods. In this study, we extract feature sets based on different combinations and configurations of spatial filters. In this research work, feature sets have been significantly reduced to only twelve components and applied to construct an effective supervised machine learning model.

### **3 Proposed Method and Model**

We propose an automatic approach for generating new sets of pixel values using different sets of filters to identify pixels in images indicative of breast cancer. Section 3.5 describes some of the filters used in this study.

#### ***3.1 Novelty in the Study***

The proposed model involves feature extraction using different filters, feature selection using the GA, feature reduction using PCA, hyperparameter optimization for the ML models, the pixel-level classification on two datasets (a) the BreCaHad dataset and (b) dataset of ultrasound images of the breast. In addition, random images are used without target labels, and the results of the proposed method are compared with the corresponding ground-truth images to visualize its performance. The assessment of our method is based on the image quality indices UIQI and structural similarity index (SSI).

### 3.2 Algorithm of the Proposed Model

**Pseudo-code:** The proposed algorithm is provided below.

---

**Input:** Dataset  $D = (x_i, y_i)$ ,  $x_i$  is the set of features of images of breast cancer patients and  $y_i$  is the set of the respective pixel values of the ground-truth images. Also used are sets of classifier models and two datasets: BreCaHad and a dataset of ultrasound images.

**Output:** Highest accuracies Acc, UIQI and SSI values of the best model ( $ACC_{max}$ ), the predicted images, and their UIQI and SSI scores, and the segmented tumor region.

---

- (i) Load dataset  $D = (x_i, y_i)$
- (ii) Pre-process all input images
- (iii) For each Model training do:
  - (a) Extract important features from the image by using different filters and set a target class by using its ground-truth image
  - (b) Split the data into training and testing subsets
  - (c) Apply genetic programming for feature selection
  - (d) Apply the RF, DT, and extra tree classifier models
  - (e) Fine-tune the hyperparameters of the classifiers based on the assessment of the training and testing subsets
- (iv) Go to the next step if the highest accuracy has been achieved; otherwise, repeat steps (a) to (d) by changing the combination of the filter sets
- (v) Select the model with the highest accuracy ( $ACC_{max}$ )
- (vi) Randomly select an image and feed it to the proposed GA-PCA-DT model
- (vii) For each sample image:
  - (a) Apply the procedure given in step iii(a)
  - (b) Tune and align the model the classifier by training and testing subsets
  - (c) Apply genetic programming for feature selection
  - (d) Apply PCA repeatedly to identify the optimum feature set (i.e., PCA components)
  - (e) Apply the reduced set of features to the final tuned model
  - (f) Calculate the accuracy ( $ACC_{max}$ ) of each predicted image with respect to the ground-truth values
- (viii) Compare the predicted image with the ground-truth image on the quality measures.

### 3.3 Diagram of Process Flow

Fig. 1 shows the step-by-step procedure for tuning the hyperparameters of all three ML algorithms, namely, the RF, ET, and DT. The classifier with the highest accuracy was selected as the final, optimized model, and was used to classify pixels of images of patients with breast cancer (see Fig. 4 in Section 3.7).

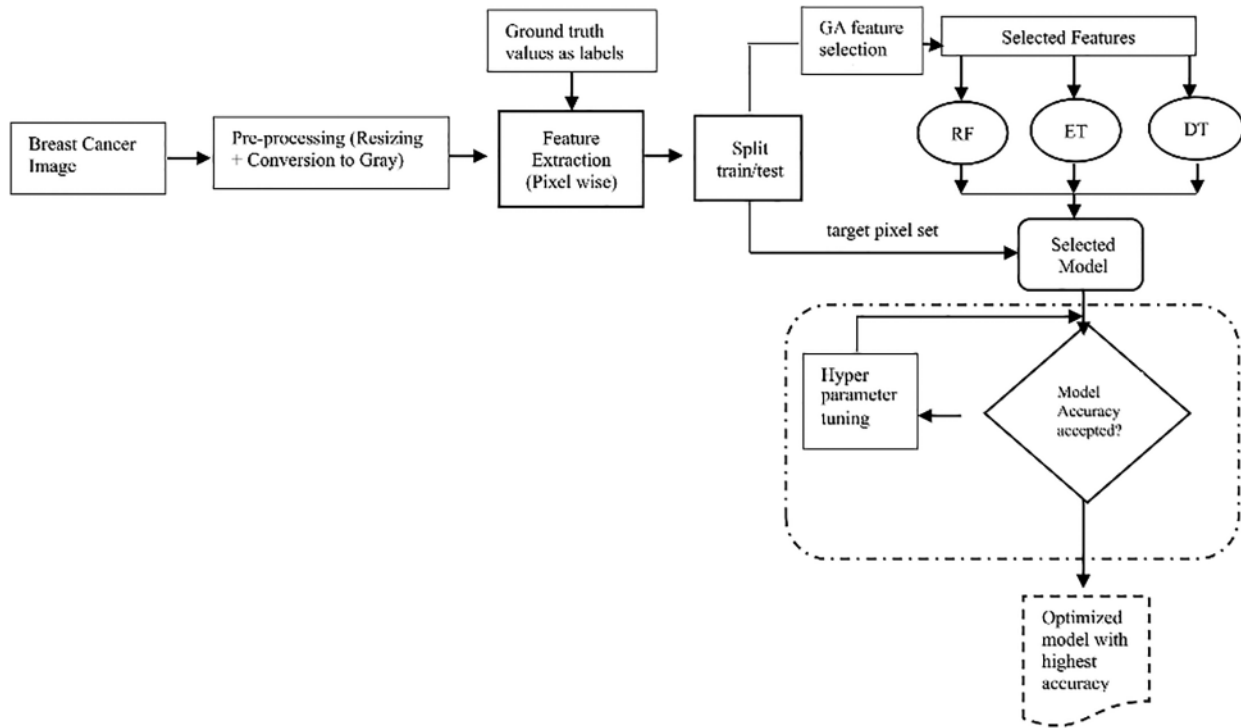


**Figure 1:** Process of hyperparameter optimization

### 3.4 Pre-Processing

Entire images of slides of tissues, of size  $1360 \times 1024$ , were converted into grayscale images of size  $300 \times 300$ . The image was resized for two reasons (a) to reduce the computational and memory-related costs, and (b) to render the image manageable.

### 3.5 Feature Extraction

#### 3.5.1 Prewitt Edge Detection Filter

Digital filters are useful for image pre-processing tasks. A variety of filters have been used in the literature to extract the properties of images [25–29]. Prewitt operators are used to detecting edges along the x and y directions to yield masks  $G_x$  and  $G_y$ , respectively.

The Prewitt operator works on grayscale images and applies both masks one by one to determine the horizontal and vertical edges. Both edges are then combined to display the complete edges of the given image:

$$G_x(x, y) = \begin{bmatrix} -1 & 0 & 1 \\ -1 & 0 & 1 \\ -1 & 0 & 1 \end{bmatrix} \times \text{Im} \quad \text{and} \quad (1)$$

$$G_y(x, y) = \begin{bmatrix} -1 & -1 & -1 \\ 0 & 0 & 0 \\ 1 & 1 & 1 \end{bmatrix} \times \text{Im} \quad (2)$$

Here  $I_m$  is an image and the total magnitude in both directions can be calculated as

$$G = \sqrt{G_x^2 + G_y^2} \quad (3)$$

A higher value of  $G$  represents better edge detection. The direction ( $D$ ) can be also determined as  $D \in \{G_x, G_y\}$

### 3.5.2 Gaussian Filter

Gaussian blurring is a method of image denoising that is commonly used for image pre-processing. The Gaussian operator for a 2D distribution is as follows:

$$G(x, y) = \frac{1}{2\pi\sigma^2} e^{-\frac{x^2+y^2}{\sigma^2}} \quad (4)$$

The value of sigma is important as it determines the width of the kernel image to be blurred. Higher values blur images over a larger area and lower values are used to limit this blurring area.

### 3.5.3 Gabor Filter

The Gabor filter acts as a local bandpass filter to extract spatial and edge-related features. It is constructed by using a Gaussian function in combination with a sinusoidal input. The filter can be expressed using parameters revised as eq (5) made more generalized, where  $\theta$  represents the orientation of the filter, the sinusoidal radial frequency is  $W$ , and  $\sigma_x, \sigma_y$  are the standard deviations. Different Gabor filters can be constructed by changing the values of the parameters. Parameter settings are crucial for identifying the patterns.

$$G(x, y) = \frac{1}{2\pi\sigma_x\sigma_y} \exp\left(-\frac{1}{2} \left[ \frac{x_k^2}{\sigma_x^2} + \frac{y_k^2}{\sigma_y^2} \right]\right) \cdot \exp[i(2\pi Wx_k + \Psi)] \quad (5)$$

where  $x_k = x\cos\theta + y\sin\theta$

and  $y_k = y\cos\theta - x\sin\theta$

$\Psi$  represents the phase shift as  $\frac{\pi}{2}, \frac{\pi}{4}, \dots$

### 3.5.4 Median Filter

The median filter is a non-linear digital filter that is commonly used to de-noise images. The median operation uses the median value of the pixels surrounding the pixel of interest. All pixel values are arranged and their median value is then selected as the value of the central pixel. Fig. 2 illustrates this process.



**Figure 2:** The median filter

### 3.6 GA-Based Feature Selection

This study uses the genetic algorithm (GA) to control the problem of dimensionality. The GA algorithm can search for the optimum value based on the survival-of-the-fittest theory. Genetic operators include selection, crossover, and mutation. These operators are applied to chromosomes (solutions) to optimize their fitness values. Chromosomes collections of genes as shown in Fig. 3a, where each gene represents a feature. For example, chromosome  $C = \{gene_1, gene_2, \dots, gene_n\}$  represents different intensities obtained from different combinations of filters.

In the feature selection, “0” indicates the absence of a particular feature in the chromosome and “1” represents its presence. The initial population size, number of generations (iterations), crossover points, crossover probability, mutation probabilities, and techniques of chromosome selection are major considerations in this vein. The process of genetic programming is shown in Fig. 3b.

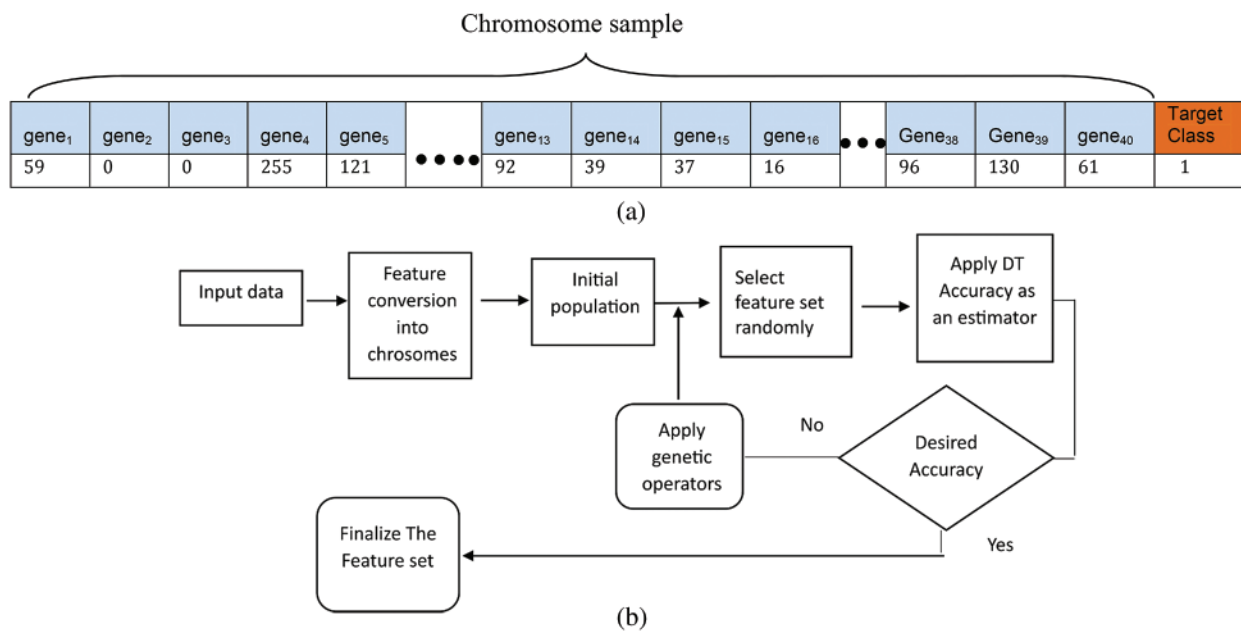


**Figure 3:** (a) Illustration of a sample chromosome. (b) Step-by-step process of GA-based feature selection

### 3.7 Principal Component Analysis (PCA)

The principal component analysis is a popular approach for dimension reduction in which an original set of attributes is orthogonally transformed into a new set of attributes. The relationship between the attribute sets (x, y) can be analyzed by a covariance matrix. Eigenvalues and eigenvectors are the fundamental measures used to determine the relevant components. The highest eigenvector with the maximum eigenvalue represents the first component, and the other components are calculated in decreasing order of value:

$$Cov_{x,y} = \frac{1}{n-1} \sum_{i=0}^n (x_i - x_m) (y_i - y_m) \tag{6}$$

where,  $I = 0, 1, \dots, n$ , and  $x_i$  is the value of the  $i^{th}$  attribute and  $x_m$  is the mean of the attribute values.  $y_i$  and  $y_m$  are the  $i^{th}$  and the mean values of the second attribute set, respectively, and are used to

calculate values of the eigenvector ( $e$ ).  $I$  refer to an identity matrix, and  $\lambda$  represents the eigenvalues and eigenvectors obtained using  $Ae = \lambda e$ . The complete eigenvectors corresponding to the eigenvalues can be found using Eq. (7).  $A$  is a covariance matrix:

$$(A - \lambda_i I) e_i = 0 \quad (7)$$

### 3.8 Supervised Classifiers

Machine learning algorithms are used to identify the important characteristics in a given dataset for predictive analysis or classification. This kind of identification is based on such attributes as the number of dimensions and the location of each data point. Medical images captured by advanced medical equipment provide a greater number and variety of features than images obtained by using traditional systems.

Fig. 4 shows the process of classifying each pixel of a given image into two essential categories, i.e., normal and cancerous.

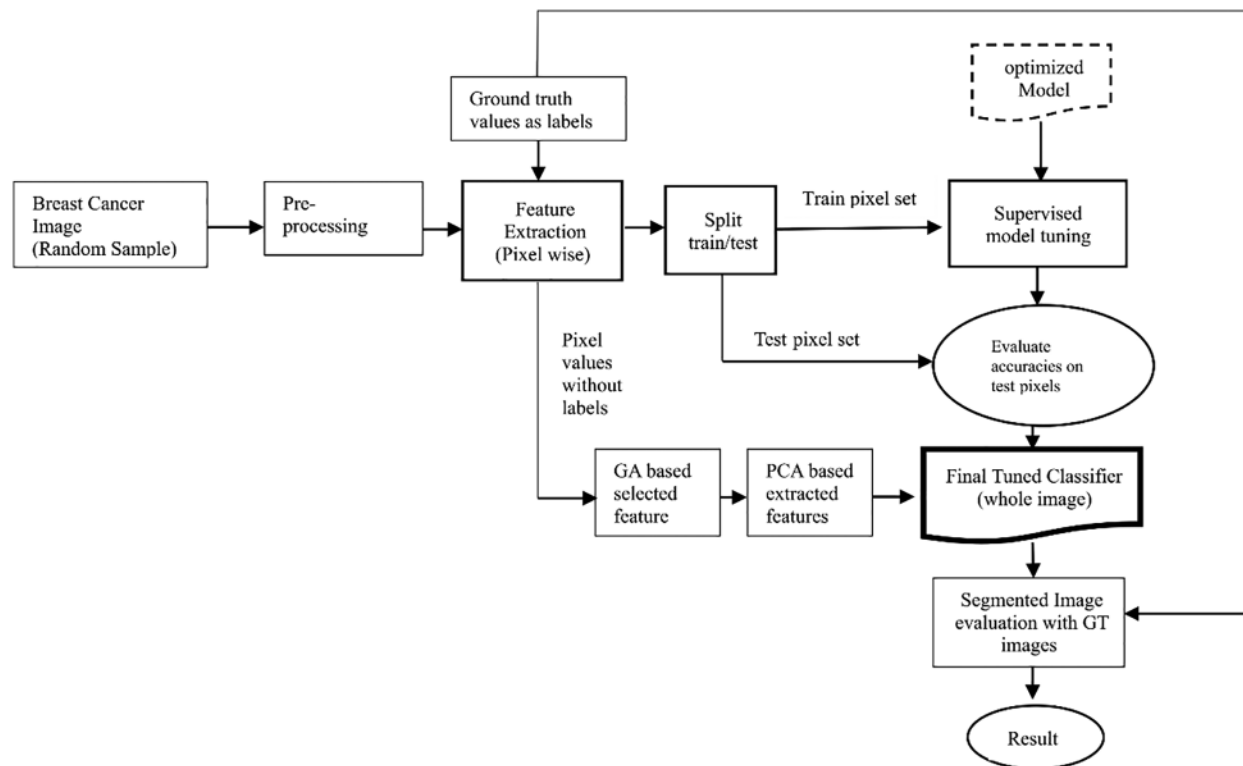


**Figure 4:** Pixel-level classification

The major steps are as follows: A random image is selected for classification. Features are extracted using a set of filters, and target values are assigned. Then the extracted dataset is split into training and testing subsets. Both subsets are submitted to the selected model. Training subset is useful to train the model for predicting each pixel value, whereas test subset result directs to tune and evaluate the model for better accuracy.

The final step consists of optimization using the genetic algorithm (GA) and principal component analysis (PCA). First, the GA selects the most discriminant and important feature set, which is

processed by PCA to be limited to 12 components. Next, the tuned and aligned models are provided with the final components without their target values. The predicted values are then compared with the respective ground-truth values.

### 3.8.1 *Random Forest (RF)*

The RF classifier uses multiple decision trees to generate different sets of samples and calculates their average accuracy. Bootstrapping is carried out and random features are selected to this end, and the final decisions are taken according to the maximum voting principle. Such averaging is useful for handling the problem of model overfitting.

### 3.8.2 *Decision Tree (DT)*

The decision tree is used to evaluate data points on pre-specified, multiple “if-else” conditions. The end nodes contain a class of all possible classes.

### 3.8.3 *Extra Tree (ET)*

This classifier is similar to the random forest and applies multiple decision trees. In the extra tree classifier, all points are supplied to the tree, whereas subsamples are supplied in the RF.

## 3.9 *Model Performance*

### 3.9.1 *Accuracy*

True positive (TP) = number of positive samples correctly predicted.

False-negative (FN) = number of positive samples incorrectly predicted.

False-positive (FP) = number of negative samples incorrectly predicted as positive.

True negative (TN) = number of negative samples correctly predicted.

Accuracy (overall): the ratio of all correctly classified cases to the total number of cases. It is defined as

$$= (TP + TN)/(TP + FP + TN + FN) \quad (8)$$

### 3.9.2 *Image Quality Assessment*

The predicted images are assessed using two image quality measures (a) Universal image quality index (UIQI) and Structural similarity index (SSI) [30,31]. Both quality measures have been discussed in Sections 4.4.1 and 4.4.2 respectively.

## 4 **Experiments and Results**

### 4.1 *Datasets*

We used the breast cancer histopathological annotation and diagnosis dataset (BreCaHAD). It is a collection of open-source, benchmark histopathological images of patients with breast cancer [32]. All images were obtained from case studies on surgical pathology. The slides were developed by H&E staining and the images were annotated. All images were available in eight-bit RGB color and had a size of 1360 × 1024 pixels. All biopsy images were classified into six malignant classes—mitosis, apoptosis, tumor nuclei, tubule, and non-tubule. Various settings were used to gather the histological structures with distinct boundaries to weakly define the histological structures. The dataset is available at <https://doi.org/10.6084/m9.figshare.7379186>.

Another dataset consisting of ultrasound images was used. These images were classified as benign, malignant, or normal. The ground-truth values of each image are also provided in this open dataset, which can be accessed at the following link: [BreastUltrasoundImagesDataset|Kaggle \[33\]](#). The dataset contained 600 images of patients with breast cancer, aged 25 to 75 years. All images had a size of  $500 \times 500$  pixels in png format. The dataset also contained ground-truth images.

#### 4.2 Experimental Setup

All experimental work was carried out by using the Google Colab cloud platform on the Tesla P100-PCIE GPU. Various Scikit learn and other packages were installed as required. The scripting language was Python 3.5 and the seed value was set to 42.

#### 4.3 Model Selection and Optimization

[Tab. 1](#) represents the optimized hyperparameter values used for model learning. The model was trained and tested using all the extracted features, a total of 40, through different combinations and configurations of eight filters.

**Table 1:** Model performance and hyperparameter values (Extracted features = 40; the number of filters applied = 8)

Model	Training accuracy	Test accuracy	Remarks (best parameter values)
Random forest	1.0	0.651	{n_estimators: 70, random_state: 50}
Decision tree	1.0	0.942	{max_depth: 100, random_state: 10}
Extra tree	0.829	0.536	{n_estimators: 500, random_state: 50}

[Tab. 2](#) shows the features extracted as well as the training and testing accuracies of the models considered. It shows that the DT provided the highest accuracy.

**Table 2:** The sets of features, and the training and testing accuracies of the RF, DT, and ET classifiers

Feature set	Extracted features	Classifier	Training accuracy	Test accuracy
Feature set-1	Gabor features	RF	1.0	0.578
		DT	1.0	0.94
		ET	0.713	0.49
Feature set-2	Gabor features+ Prewitt	RF	1.0	0.581
		DT	1.0	0.941
		ET	0.716	0.468
Feature set-3*	Gabor features+Prewitt +Gaussian	RF	1.0	0.658
		DT	<b>1.0</b>	<b>0.942</b>
		ET	0.785	0.575
Feature set-4	Gabor+ Prewitt+Gaussian+ Median features	RF	1.0	0.69
		DT	1.0	0.94
		ET	0.82	0.60

Tab. 2 shows that feature set-3 provided an accuracy of 0.942 by using only 36 features with the decision tree classifier. Feature set-3 was then supplied to the genetic algorithm for feature selection and reduction, and yielded only 30 prominent features. The pixel value of the original image has also been extracted as one of the features. The values of the GA operator were set as follows: population = 10, crossover probability = 0.5, mutation probability = 0.2, generation = 5, and tournament size = 3. The population and the number of generated values were reduced to minimize the computational cost. A lower probability of mutation was better for avoiding the local minimum. The reduced feature set obtained by the GA operator was fed to all three classifiers. The 30 features thus selected increased the testing accuracy by 0.1% (from 0.942 to 0.943). The accuracies of all classifiers are shown in Tab. 3.

**Table 3:** The accuracy values obtained by using GA-based features

Classifiers	GA-DT model (30 features)		Base models (36 features)	
	Training accuracy	Test accuracy	Training accuracy	Test accuracy
DT	1.0	<b>0.9431</b>	1.0	0.942

When classifying the images, the population was set to 50 and the number of generations to 20 to ensure robust performance. The seed value was set to 42 to ensure that the results could be reproduced, and the components of PCA were limited to 12. This yielded a range of variance of 0.9999 to 1.0.

**4.4 Strategy for Image Evaluation**

To evaluate the images, an unlabeled image was first supplied to build the model (GA-PCA-DT) and the output of the model (predicted image) was compared with the respective ground-truth (labeled) image. The markers or labels of the predicted and the ground-truth images were then noted. The relevant steps are shown in Fig. 5.

To check the robustness of the model, one image from each malignant class was randomly selected and supplied to it for label prediction. Tab. 4 lists the images predicted by the GA-PCA-DT model and the corresponding ground-truth images. Tab. 5 shows the pixel-level accuracies.

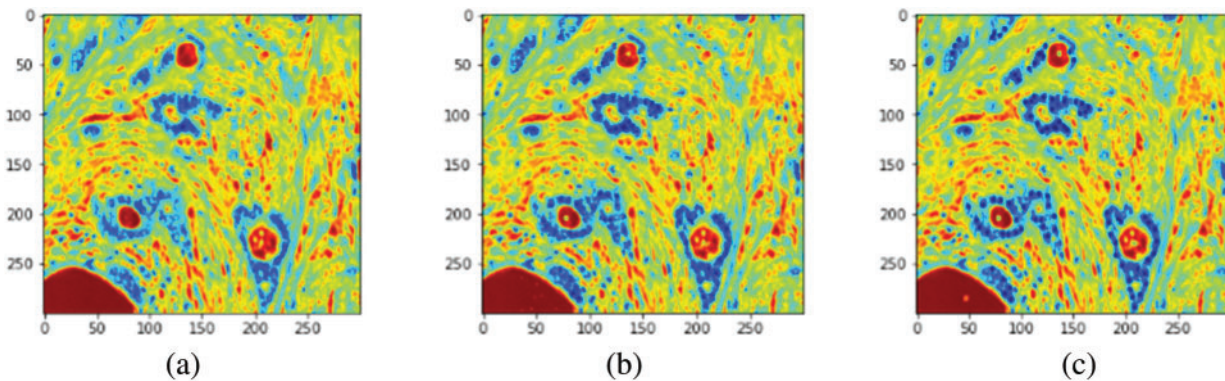


**Figure 5:** (Continued)

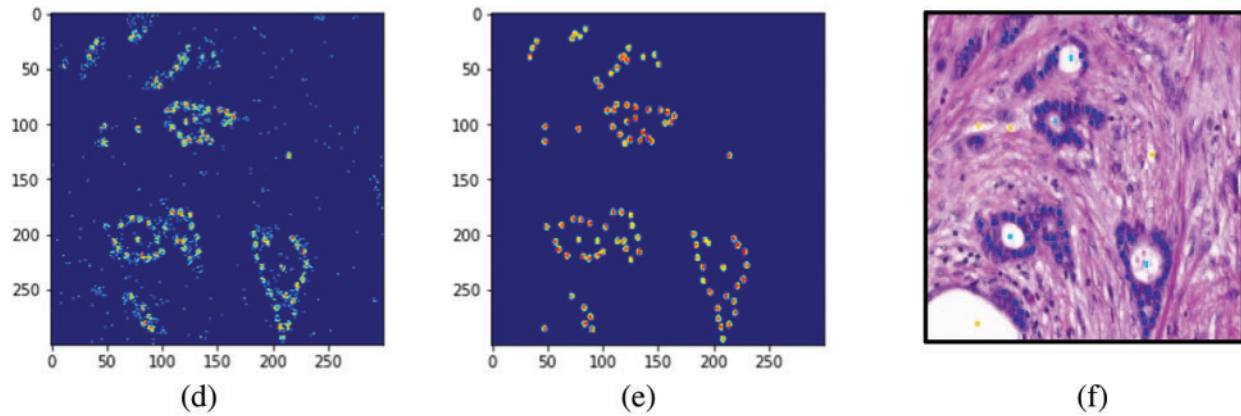


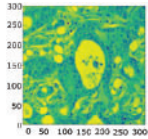
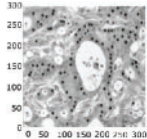
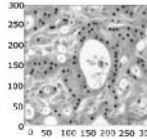
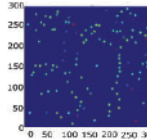
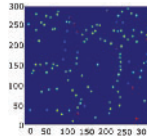
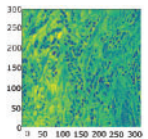
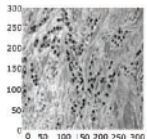
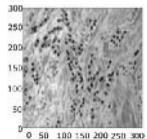
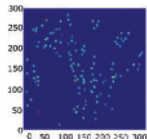
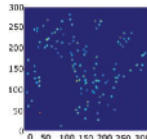
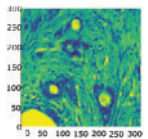
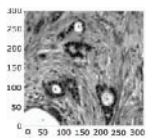
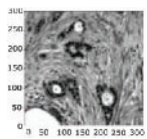
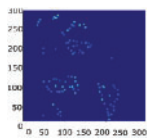
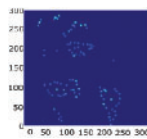
**Figure 5:** Processing histopathology images. (a) Resized original image ( $300 \times 300$ ). (b) The image was generated using the proposed GA-DT model. (c) The ground-truth image. (d) Labels assigned by the GA-DT model (e) Labels marked in the ground-truth image. (f) Original annotated image (in RGB)

**Table 4:** Comparison between the images predicted by the proposed model and the relevant ground-truth images for the BreCaHad dataset

Image ID	Original image (in BGR)	Ground-truth image (in grayscale)	Predicted image (in grayscale)	Ground-truth nucleus annotation (in “jet” colormap)	Predicted nucleus annotation using GA+PCA (12)* features+DT (in “jet” colormap)
Image Case_1-04.png					
Image Case_12-09.png					
Image Case_13-05.png					

(Continued)

**Table 4:** Continued

Image ID	Original image (in BGR)	Ground-truth image (in grayscale)	Predicted image (in grayscale)	Ground-truth nucleus annotation (in “jet” colormap)	Predicted nucleus annotation using GA+PCA (12)* features+DT (in “jet” colormap)
Image Case_16-03.png					
Image Case_17-06.png					
Image Case_4-10.png					

Note: \*PCA(12) = PCA first 12 components.

**Table 5:** Pxl-level classification accuracies delivered by the GA+PCA+DT model with and without using the feature selection methods GA/PCA

Image	Training/Testing and whole-image accuracies	Accuracy using GA features (24 features)	Whole-image accuracy with GA+PCA (12) features	PCA variance with 12 components
Image Case_1-04.png	Train: 1.0 Test: 0.9418 Whole image 1.0	Train: 1.0 Test: 0.94227 Whole image: 1.0	Whole image:1.0	0.99996
Image Case_12-09.png	Train: 1.0 Test: 0.91844 Whole image 1.0	Train: 1.0 Test: 0.92013 Whole image: 1.0	Whole image:1.0	0.99997
Image Case_13-05.png	Train: 1.0 Test: 0.94897 Whole image 1.0	Train: 1.0 Test: 0.94836 Whole image: 1.0	Whole image:1.0	1.0

(Continued)

**Table 5:** Continued

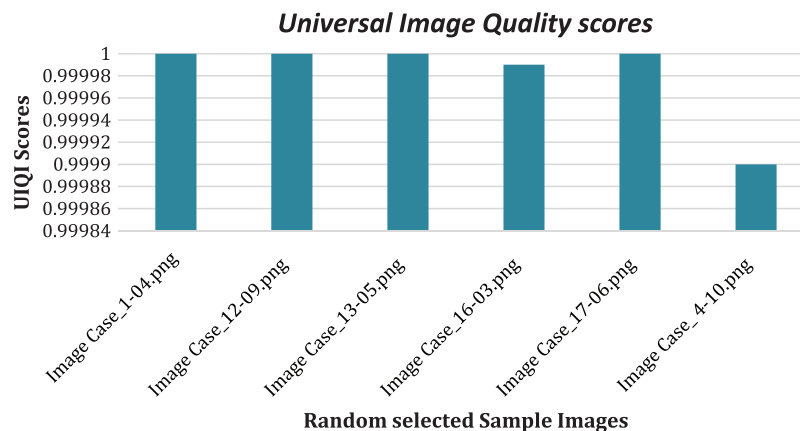
Image	Training/Testing and whole-image accuracies	Accuracy using GA features (24 features)	Whole-image accuracy with GA+PCA (12) features	PCA variance with 12 components
Image Case_16-03.png	Train: 1.0 Test: 0.93902 Whole image 1.0	Train: 1.0 Test: 0.99988 Whole image: 1.0	Whole image:0.999788	0.99999
Image Case_17-06.png	Train: 1.0 Test: 0.94544 Whole image 1.0	Train: 1.0 Test: 0.94711 Whole image: 1.0	Whole image:1.0	0.99999
Image Case_4-10.png	Train: 0.99962 Test: 0.95802 Whole image: 0.99994	Train: 0.99974 Test: 0.957166 Whole image: 0.99978	Whole image: 0.99978	0.99995

#### 4.4.1 Graphical Illustration of UIQI

A simplified image quality measure, UIQI, has been proposed by Wang and Bovik. UIQI evaluates the quality of the test image over the referenced image by finding, loss in correlation, distortions in luminance and distortions in contrast. For example, suppose,  $I_m$  and  $I_r$  are two images. Then UIQI value will be the product of all the above three components mathematically expressed as given in the reference [30]:

$$UIQI(I_m, I_r) = \frac{\sigma_{I_m I_r}}{\sigma_{I_r} \sigma_{I_m}} \cdot \frac{2 \overline{I_m I_r}}{(\overline{I_m})^2 + (\overline{I_r})^2} \cdot \frac{2 \cdot \sigma_{I_r} \sigma_{I_m}}{\sigma_{I_r}^2 + \sigma_{I_m}^2} \quad (9)$$

UIQI has been employed to evaluate how the predicted images corresponded to the ground-truth images, as shown in Fig. 6.

**Figure 6:** UIQI scores of the predicted images

#### 4.4.2 Graphical Comparison Based on SSI

An extension of the UIQI, structural similarity (SSI), was also proposed by Wang et al. [30,31]. The SSI is commonly used in videos and still images. It evaluates the degradation in image quality caused by pre-processing or losses in transmission. It uses two images to this end, i.e., the original and the processed image.

The SSI examines the similarity between the original and the processed image. It has a value between zero and one, where zero indicates that the images are completely dissimilar, and one indicates that they are identical. The SSI measure assumes that the human eye gathers image information through three channels, luminance, contrast, and structure present in the images. Therefore, SSI uses measurement functions for luminance (L), contrast (C), and structure (S). These functions are combined to calculate the final SSI value as represented in Eq. (10). Suppose  $I_m$  and  $I_r$  are two images. To compare their image quality measure, SSI can be expressed as follows.

$$SSI(I_m, I_r) = f(L(I_m, I_r)) \cdot C(I_m, I_r) \cdot S(I_m, I_r) \quad (10)$$

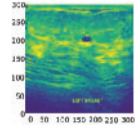
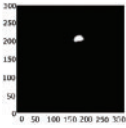
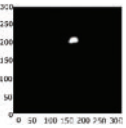
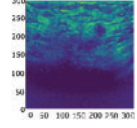
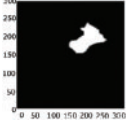
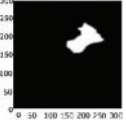
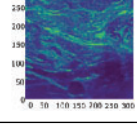
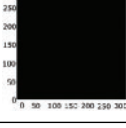
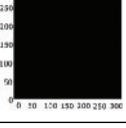
A score of 0.99 and above is considered representative of satisfactory similarity. The SSI scores of the randomly selected images are shown in Fig. 7.



**Figure 7:** Structural similarity scores

Tab. 6 shows the classification-related performance of the proposed model based on the dataset of ultrasound images. Total extracted features are limited to 12 components using PCA and supplied to Decision Tree. The maximum accuracy pixel-level classification was obtained 1.0 for each test sample.

**Table 6:** Comparison between the predicted images and the relevant ground-truth images from the ultrasound breast cancer tumor dataset

Image class and ID (random sample from each class)	Original image (In BGR format)	Ground-truth Image**	Predicted image GA+PCA (12)+DT features)**	Feature importance using GA+PCA (12)	Whole-image accuracy using GA+PCA (12)+DT
<b>(i) Benign Class</b> benign (1) .png				1.0	1.0
<b>(ii) Malignant Class</b> malignant (147)				1.0	1.0
<b>(iii) Normal Class</b> normal (85) .png				1.0	1.0

Note: \*\* Black and white images.

## 5 Conclusion and Future Work

The proposed method successfully extracted prominent spatial features from the images through various filters, reduced feature set size by implementing GA and PCA in the combination, and accurately classified all pixels of chosen test images. The RF, DT, and extra tree models were built, and their hyperparameters were optimized based on the training and testing sets. The training accuracies of the GA-based method (without PCA) was 1.0, and testing accuracies ranged from 0.92 to 0.99 for the histopathology dataset. In the ultrasound image dataset, the model yielded training accuracies of 1.0 and testing accuracies from 0.9327 to 1.0. The final proposed model, GA-PCA-DT, was tested on images selected from each class. The proposed model has produced whole image classification accuracy between 0.9997 and 1.0. Furthermore, the predicted image (all pixels values) compared with respective ground-truth values generated UIQI scores in the range of 0.9999 to 1.0 and SSI scores in the range of 0.99824 to 1.0 for the test images, chosen randomly from every class of both datasets.

Breast cancer detection and annotation is a tedious and time-consuming task for every healthcare expert. The proposed model is simple, accurate, fast, and inexpensive, and thus can help classify whole image pixels into binary classes i.e., “disease” and “non-disease”. We believe that healthcare expert’s interventions are necessary for every medical examination and such automatic models can only assist experts at the primary level in expediting breast cancer detection, especially in the large populations or remote areas where healthcare facility is not sufficient.

The results reported here are excellent but slightly overfitted. The likely reasons for this are (a) a large number of target classes and (b) the consideration of exceptional pixel values as an additional class. The problem of overfitting can be solved by increasing the population size, further fine-tuning the model, and using regularization methods.

In future work, attention can be drawn to the use of more ML models, filters, and the employment of feature reduction techniques. In addition, different image quality measures can be explored to determine better evaluation. In this study, the images were resized to lower dimensions. Future studies can consider operations on the original images (i.e.,  $1360 \times 1024$ ), and RGB (i.e., red, green, blue) channels should be used instead of grayscale values.

**Acknowledgement:** The authors thank the following dataset contributors:

- (a) We thank Aksac et al. for providing a histopathological annotated dataset for breast cancer diagnosis for academic and research purposes, available at <https://doi.org/10.6084/m9.figshare.7379186> (last accessed 31.01.22).
- (b) We also used ultrasound images for breast cancer diagnosis from the Breast Ultrasound Images Dataset | Kaggle.

**Funding Statement:** The authors received no funding for this study.

**Conflicts of Interest:** The authors declare that they have no conflicts of interest to report regarding the publication of this study.

## References

- [1] R. L. Siegel, K. D. Miller, H. E. Fuchs and A. Jemal, "Cancer statistics," *CA: A Cancer Journal for Clinicians*, vol. 71, no. 1, pp. 7–33, 2021.
- [2] M. M. Sunilkumar, C. G. Finni, A. S. Lijimol and M. R. Rajagopal, "Health-related suffering and palliative care in breast cancer," *Current Breast Cancer Reports*, vol. 13, no. 4, pp. 241–246, 2021.
- [3] R. Wazirali and R. Ahmed, "Hybrid feature extractions and CNN for enhanced periocular identification during COVID-19," *Computer Systems Science and Engineering*, vol. 41, no. 1, pp. 305–320, 2022.
- [4] P. Filipczuk, B. Krawczyk and M. Woźniak, "Classifier ensemble for an effective cytological image analysis," *Pattern Recognition Letters*, vol. 34, no. 14, pp. 1748–1757, 2013.
- [5] G. Reshma, C. A. Atroshi, V. K. Nassa, B. T. Geetha, G. Sunitha *et al.*, "Deep learning-based skin lesion diagnosis model using dermoscopic images," *Intelligent Automation & Soft Computing*, vol. 31, no. 1, pp. 621–634, 2022.
- [6] S. Mane and S. Shinde, "A method for melanoma skin cancer detection using dermoscopy images," in *2018 Fourth Int. Conf. on Computing Communication Control and Automation (ICCCUBEA)*, Pune, India, pp. 1–6, 2018.
- [7] A. B. Tosun, M. Kandemir, C. Sokmensuer and C. Gunduz-Demir, "Object-oriented texture analysis for the unsupervised segmentation of biopsy images for cancer detection," *Pattern Recognition*, vol. 42, no. 6, pp. 1104–1112, 2009.
- [8] A. V. Alvarenga, W. C. A. Pereira, A. F. C. Infantosi and C. M. Azevedo, "Complexity curve and grey level co-occurrence matrix in the texture evaluation of breast tumor on ultrasound images: Texture evaluation of breast tumor on ultrasound images," *Medical Physics*, vol. 34, no. 2, pp. 379–387, 2007.
- [9] M. Moradi, P. Abolmaesumi, D. R. Siemens, E. E. Sauerbrei, A. H. Boag *et al.*, "Augmenting detection of prostate cancer in transrectal ultrasound images using SVM and RF time series," *IEEE Transactions on Biomedical Engineering*, vol. 56, no. 9, pp. 2214–2224, 2009.
- [10] R. S. Xu, O. Michailovich and M. Salama, "Information tracking approach to segmentation of ultrasound imagery of the prostate," *IEEE Transactions on Ultrasonics, Ferroelectrics and Frequency Control*, vol. 57, no. 8, pp. 1748–1761, 2010.

- [11] S. Karacavus, B. Yilmaz, A. Tasdemir, O. Kayaalti, E. Kaya *et al.*, “Can laws be a potential PET image texture analysis approach for evaluation of tumor heterogeneity and histopathological characteristics in NSCLC?,” *Journal of Digital Imaging*, vol. 31, no. 2, pp. 210–223, 2018.
- [12] M. Wu, R. F. Fraser and C. W. Chen, “A novel algorithm for computer-assisted measurement of cervical length from transvaginal ultrasound images,” *IEEE Transactions on Information Technology in Biomedicine*, vol. 8, no. 3, pp. 333–342, 2004.
- [13] M. M. R. Krishnan, V. Venkatraghvan, U. R. Acharya, M. Pal, R. R. Paul *et al.*, “Automated oral cancer identification using histopathological images: A hybrid feature extraction paradigm,” *Micron*, vol. 43, no. 2, pp. 352–364, 2012.
- [14] B. S. Garra, B. H. Krasner, S. C. Horii, S. Ascher, S. K. Mun *et al.*, “Improving the distinction between benign and malignant breast lesions: The value of sonographic texture analysis,” *Ultrasonic Imaging*, vol. 15, no. 4, pp. 267–285, 1993.
- [15] O. S. Al-Kadi, “Texture measures combination for improved meningioma classification of histopathological images,” *Pattern Recognition*, vol. 43, no. 6, pp. 2043–2053, 2010.
- [16] W. Gomez, W. C. A. Pereira and A. F. C. Infantosi, “Analysis of co-occurrence texture statistics as a function of gray-level quantization for classifying breast ultrasound,” *IEEE Transactions on Medical Imaging*, vol. 31, no. 10, pp. 1889–1899, 2012.
- [17] Y. -L. Huang, K. -L. Wang and D. R. Chen, “Diagnosis of breast tumors with ultrasonic texture analysis using support vector machines,” *Neural Computing and Applications*, vol. 15, no. 2, pp. 164–169, 2006.
- [18] Y. -L. Huang, D. -R. Chen and Y. -K. Liu, “Breast cancer diagnosis using image retrieval for different ultrasonic systems,” in *2004 Int. Conf. on Image Processing. ICIP '04*, Singapore, vol. 5, pp. 2957–2960, 2004.
- [19] R. Rashmi, K. Prasad, C. B. K. Udupa and V. Shwetha, “A comparative evaluation of texture features for semantic segmentation of breast histopathological images,” *IEEE Access*, vol. 8, no. 1, pp. 64331–64346, 2020.
- [20] F. A. Spanhol, L. S. Oliveira, C. Petitjean and L. Heutte, “A dataset for breast cancer histopathological image classification,” *IEEE Transactions on Biomedical Engineering*, vol. 63, no. 7, pp. 1455–1462, 2016.
- [21] D. Kramer and F. Aghdasi, “Texture analysis techniques for the classification of microcalcifications in digitised mammograms,” in *1999 IEEE Africon. 5th Africon Conf. in Africa (Cat. No.99CH36342)*, Cape Town, South Africa, pp. 395–400, 1999.
- [22] H. Soltanian-Zadeh, S. Pourabdollah-Nezhad and F. Rafiee Rad, “Shape-based and texture-based feature extraction for classification of microcalcifications in mammograms,” in *Proc. SPIE 4322, Medical Imaging 2001*, San Diego, CA, pp. 301–310, 2001.
- [23] R. Kumar, R. Srivastava and S. Srivastava, “Microscopic biopsy image segmentation using hybrid color K-means approach,” *International Journal of Computer Vision and Image Processing*, vol. 7, no. 1, pp. 79–90, 2017.
- [24] A. Khanna, N. D. Londhe and S. Gupta, “Automatic lung segmentation and airway detection using adaptive morphological operations,” in *Machine Intelligence and Signal Analysis*, In: M. Tanveer, R. B. Pachori (eds.), Vol. 748. Singapore: Springer, pp. 347–354, 2019.
- [25] X. Li and K. N. Plataniotis, “A complete color normalization approach to histopathology images using color cues computed from saturation-weighted statistics,” *IEEE Transactions on Biomedical Engineering*, vol. 62, no. 7, pp. 1862–1873, 2015.
- [26] P. -W. Huang and Y. -H. Lai, “Effective segmentation and classification for HCC biopsy images,” *Pattern Recognition*, vol. 43, no. 4, pp. 1550–1563, 2010.
- [27] Z. Wang and W. T. Ang, “Automatic dissection position selection for cleavage-stage embryo biopsy,” *IEEE Transactions on Biomedical Engineering*, vol. 63, no. 3, pp. 563–570, 2016.
- [28] R. Sarkar and S. T. Acton, “SDL: Saliency-based dictionary learning framework for image similarity,” *IEEE Transactions on Image Processing*, vol. 27, no. 2, pp. 749–763, 2018.

- [29] M. Sapkota, F. Liu, Y. Xie, H. Su, F. Xing *et al.*, “AIIMDs: An integrated framework of automatic idiopathic inflammatory myopathy diagnosis for muscle,” *IEEE Journal of Biomedical and Health Informatics*, vol. 22, no. 3, pp. 942–954, 2018.
- [30] Z. Wang and A. C. Bovik, “A universal image quality index,” *IEEE Signal Processing Letters*, vol. 9, no. 3, pp. 81–84, 2002.
- [31] M. Oszust, “Full-reference image quality assessment with linear combination of genetically selected quality measures,” *PLOS ONE*, vol. 11, no. 6, pp. 1–17, 2016.
- [32] A. Aksac, D. J. Demetrick, T. Ozyer and R. Alhajj, “BreCaHAD: A dataset for breast cancer histopathological annotation and diagnosis,” *BMC Research Notes*, vol. 12, no. 82, pp. 1–3, 2019.
- [33] W. A. Dhabyani, M. Gomaa, H. Khaledand and A. Fahmy, “Dataset of breast ultrasound images,” *Data in Brief*, vol. 28, no. 1, pp. 104863, 2020.